Photoelectrochemistry with Integrated Photosensitizer−Electron Acceptor and Au-Nanoparticle Arrays

Michal Lahav,[†] Vered Heleg-Shabtai,[†] Julian Wasserman,[†] Eugenii Katz,[†] Itamar Willner,*[,†] Heinz Dürr,[‡] Yi-Zhen Hu,[‡] and Stefan H. Bossmann[§]

Contribution from the Institute of Chemistry and The Farkas Center for Light-Induced Processes, The Hebrew University of Jerusalem, Jerusalem 91904, Israel, FR 11.2 Organische Chemie, Universität des Saarlandes, 66041 Saarbrücken, Germany, and Engler-Bunte Institut der Universität Karlsruhe, 76128 Karlsruhe, Germany

Received July 13, 2000

Abstract: Photosensitizer/electron acceptor molecular cross-linked Au-nanoparticle arrays are assembled on indium-doped tin oxide (ITO) electrodes by a layer-by-layer deposition process. A Ru(II)−tris-(2,2′-bipyridine)-cyclobis(paraquat-*p*-phenylene) catenane (**1**) or Zn(II)-protoporphyrin IX−bis(*N*-methyl-*N*′-undecanoate-4,4′-bipyridinium) (**2**) are used as molecular cross-linkers for the generation of Au-nanoparticle (13 ± 1 nm) arrays of a controlled number of layers. The Au-nanoparticle arrays are characterized by absorbance spectroscopy and by electrochemical means. The electrodes functionalized with **1**- or **2**-cross-linked Au-nanoparticle arrays are used in photoelectrochemical experiments. The resulting action spectra of the photocurrents follow the absorbance spectra of the respective chromophores. Mechanistic studies indicate that the photocurrents originate from intramolecular electron-transfer quenching of the photoexcited state of the photosensitizer by the electron acceptor units, leading to the formation of intermediate redox species. The oxidized photoproduct oxidizes the sacrificial electron donor, Na_2EDTA, whereas the reduced bipyridinium radical cations transfer the electrons to the bulk electrode support.

Nanoparticle architectures[1] on electrode supports attract substantial research efforts directed to the development of photoelectrochemical or solar cells.[2] Semiconductor nanoparticle arrays assembled on electrodes were employed as active interfaces for photocurrent generation.[3] The coupling of two semiconductors such as CdS/TiO_2 CdS/AgI, or ZnS/TiO_2 facilitates interparticle electron transfer and charge separation.[4] Bridging of different semiconductor particles by molecular units was employed to generate novel photoelectrochemical systems.[5] For example, CdS and TiO_2 particles bridged by a bifunctional thiol-carboxylic acid spacer reveal efficient photoinduced interparticle charge separation. Sensitization of nanoporous semiconductors by organic dyes[6] or transition metal complexes[7] has been widely employed for the switching of semiconductor activities to the visible-light region. Photosensitization of rough nanoporous TiO_2 films by layers of Ru(II)−polypyridine complexes was widely examined for the production of high-efficiency solar cells.[8]

Metal-nanoparticle arrays reveal unique photonic,[9] electronic,[10] and nonlinear optical[11] properties. These unique properties of nanoparticles were used to develop DNA-sensing systems[12] or assemblies with switchable conductivity.[13] In a series of recent reports we addressed the organization of layered Au-nanoparticle architectures on conductive-glass supports by cross-linking the particles with oligocationic molecular bridging

* Author for correspondence. Telephone: 972-2-6585272. Fax: 972-2-6527715. E-mail: willnea@vms.huji.ac.il.

† The Hebrew University of Jerusalem.

‡ Universität des Saarlandes.

§ Universität Karlsruhe.

(1) (a) Shipway, A. N.; Katz, E.; Willner, I. *ChemPhysChem* **2000**, *1*, 18−52. (b) Shipway, A. N.; Lahav, M.; Willner, I. *Adv. Mater.* **2000**, *12*, 993−998.

(2) (a) Kamat, P. V. In *Nanoparticles and Nanostructured Films*; Fendler, J. H., Ed.; Wiley-VCH: Weinheim, Germany, 1998; p 207. (b) Cassagneau, T.; Mallouk, T. E.; Fendler, J. H. *J. Am. Chem. Soc.* **1998**, *120*, 7848−7859. (c) Calvin, V. L.; Schlamp, M. C.; Alivisatos, A. P. *Nature* **1994**, *370*, 354−357.

(3) (a) Miyake, M.; Torimoto, T.; Sakata, T.; Mori, H.; Yonayama, H. *Langmuir* **1999**, *15*, 1503−1507. (b) Kotov, N. A.; Dékány, I.; Fendler, J. H. *J. Phys. Chem.* **1995**, *99*, 13065−13069. (c) Torimoto, T.; Tsumura, N.; Miyake, M.; Nishizawa, M.; Sakata, T.; Mori, H.; Yoneyama, H. *Langmuir* **1999**, *15*, 1853−1858. (d) Alperson, B.; Demange, H.; Rubinstein, I.; Hodes, G. *J. Phys. Chem. B* **1999**, *103*, 4943−4948.

(4) (a) Spanhel, L.; Weller, H.; Henglein, A. *J. Am. Chem. Soc.* **1987**, *109*, 6632−6640. (b) Gopigas, K. R.; Bohorquez, M.; Kamat, P. V. *J. Phys. Chem.* **1990**, *94*, 6435−6440. (c) Serpone, N.; Borgarello, E.; Grätzel, M. *J. Chem. Soc., Chem. Commun.* **1984**, 342−344. (d) Pichat, P.; Borgarello, E.; Disdier, J.; Herrmann, J. M.; Pelizzetti, E.; Serpone, N. *J. Chem. Soc., Faraday Trans. 1* **1988**, *84*, 261−274. (e) Serpone, N.; Borgarello, E.; Pelizzetti, E. *J. Electrochem. Soc.* **1988**, *135*, 2760−2766.

(5) Lawless, D.; Kapoor, S.; Meisel, D. *J. Phys. Chem.* **1995**, *99*, 10329−10335.

(6) Khazraji, A. C.; Hotchandani, S.; Das, S.; Kamat, P. V. *J. Phys. Chem. B* **1999**, *103*, 4693−4700.

(7) Grätzel, M. In *Semiconductor Nanoclusters - Physical, Chemical and Catalytic Aspects*; Kamat, P. V., Meisel, D., Eds.; Elsevier: Amsterdam, 1997; p 353.

(8) O'Regan, B.; Grätzel, M. *Nature* **1991**, *353*, 737−740.

(9) (a) Alivisatos, A. P. *Science* **1996**, *271*, 933−937. (b) Alivisatos, A. P.; Johnsson, K. P., Peng, X. G.; Wilson, T. E.; Loweth, C. J.; Bruchez, M. P., Jr.; Schultz, P. G. *Nature* **1996**, *382*, 609−611.

(10) (a) Menon, V. P.; Martin, C. R. *Anal. Chem.* **1995**, *65*, 1920−1928. (b) Bethell, D.; Brust, M.; Schiffrin, D. J.; Kiely, C. *J. Electroanal. Chem.* **1996**, *409*, 137−143. (c) Feldheim, D. L.; Keating, C. D. *Chem. Soc. Rev.* **1998**, *27*, 1−12. (d) Weller, H. *Angew. Chem., Int. Ed.* **1998**, *37*, 1658−1659.

(11) Sandrock, M. L.; Pibel, C. D.; Geiger, F. M.; Foss, C. A., Jr. *J. Phys. Chem. B* **1999**, *103*, 2668−2673.

(12) (a) Storhoff, J. J.; Elghanian, R.; Mucic, R. C.; Mirkin, C. A.; Letsinger, R. L. *J. Am. Chem. Soc.* **1998**, *120*, 1959−1964. (b) Mirkin, C. A. *Inorg. Chem.* **2000**, *39*, 2258−2272. (c) Patolsky, F.; Lichtenstein, A.; Ranjit, K. T.; Willner, I. *Chem. Commun.* **2000**, 1025−1026.

(13) Markovich, G.; Collier, C. P.; Heath, J. R. *Phys. Rev. Lett.* **1998**, *80*, 3807−3810.

10.1021/ja002568d CCC: $19.00
Published on Web 11/03/2000

units.[14,15] The molecular cross-linked nanoparticle arrays exhibit three-dimensional conductivity. By the cross-linking of Au-nanoparticle arrays with size- and shape-specific receptors, the selective electrochemical sensing of various substrates was demonstrated.[16,17] The sensitivity of the resulting receptor−Au-nanoparticle architectures can be tuned by the number of functional nanoparticle layers associated with the array.

In a preliminary study[18] we reported on the organization of an Au-nanoparticle array cross-linked by a Zn-protoporphyrin IX−bis-bipyridinium, photosensitizer− electron acceptor dyad. The optical and electrochemical properties of the assembly were characterized, and the three-dimensional conductivity of the array was used to stimulate a photocurrent by the photonic excitation of the chromophore. In the present contribution we address the organization of Au-nanoparticle arrays that are cross-linked by the Ru(II)−tris-(2,2′-bipyridine)-cyclobis(paraquat-*p*-phenylene) catenane (**1**)[19] or Zn(II)-protoporphyrin IX−bis-bipyridinium (**2**). We discuss the electrochemical and optical properties of the systems and present the photoelectrochemical features of the assemblies.

Experimental Section

Materials. Ru(II)−tris-(2,2′-bipyridine)-cyclobis(paraquat-*p*-phenylene) catenane (**1**) was synthesized according to the literature.[20]

Zn-protoporphyrin IX−bis-(*N*-methyl-N′-undecanoate-4,4′-bipyridinium) (**2**) was synthesized according to the literature[21] with changes in some synthetic steps.

Zn-protoporphyrin IX Bis(11-bromoundecyl ester) (3). To a suspension of protoporphyrin IX (0.5 g, 0.89 mmol) in CH_2Cl_2 (40 mL) was added Et_3N (1.4 mL, 9.8 mmol). The mixture was stirred at room temperature for 1 h. The red solid residue obtained by concentration was treated with $COCl_2$ (0.6 mL, 6.85 mmol) in CH_2Cl_2 (40 mL) at ambient temperature for 1 h. Concentration of the reaction mixture in vacuo to dryness gave the bis(acid chloride) derivative of protoporphyrin IX as a purple solid. A mixture of the bis(acid chloride) derivative thus obtained, $Br(CH_2)_{11}OH$ (5.73 gr, 22.8 mmol), and Et_3N (2.3 mL, 16.4 mmol) in CH_2Cl_2 (40 mL) was heated under reflux for 6 h. The concentrated residue was washed with H_2O and was chromatographed on Al_2O_3. Elution with $CHCl_3$ and subsequent evaporation yielded the protoporphyrin IX bis(11-bromoundecyl ester) as purple crystals. A saturated solution of $Zn(OAc)_2$ (279 mg, 1.27 mmol) in MeOH (7 mL) was added to the bromo ester derivative (0.8 g, 0.753 mL) in $CHCl_3$ (70 mL), and the mixture was heated under reflux for 10 min. The concentrated mixture was purified by chromatography (Al_2O_3, benzene−$CHCl_3$ (1:1)). Recrystallization from $CHCl_3$−hexane (1:1) gave **3** (0.287 g, 34%) as reddish purple crystals. ^{1}H NMR (DMSO-d_6) δ (ppm) = 8.8−9.2 (4H, protoporphyrin IX); 6.0−6.2, 7.8, 8,0 (6H, vinyl); 3.3−3.4 (12H, CH_3 on protoporphyrin IX); 2.9−4.1 (16H, $CH_2CH_2COOCH_2$, CH_2−Br); 0.7−1.2 (36H, $-(CH_2)_9-$).

Zn-protoporphyrin IX−Bis[11-(4,4′-bipyridinio)undecyl ester] Dibromide (4). A mixture of **3** (0.815 g, 0.722 mmol) and 4,4′-bipyridyl (2.26 g, 1.45 mmol) in DMF (60 mL) was heated at 100 °C for 24 h. The concentrated reddish-purple solid was washed with benzene (10 × 50 mL) and then with hexane (2 × 50 mL) to remove an excess of 4,4′-bipyridyl to give reddish-purple crystals of **4** (0.2 g, 19%). ^{1}H NMR (DMSO-d_6) δ (ppm) = 10.3 (4H, protoporphyrin IX); 7.9−9.0 (16H, bpy); 6.1, 6.4, 8.5 (6H, vinyl); 3.6, 3.7 (12H, CH_3 on protoporphyrin IX); 3.2−4.3 (16H, $CH_2CH_2COOCH_2$, CH_2-Py^+-Py); 0.8−1.26 (36H, $-(CH_2)_9-$).

Zn-protoporphyrin IX−Bis[11-[4-(1-methyl-4-pyridinio))-1-pyridinio]undecyl ester] Tetrabromide (5). A large excess of CH_3Br was bubbled through a solution of **4** (0.08 g, 0.06 mmol) at ambient temperature for 2 h. A reddish-brown solid precipitated in the flask, and this was filtered and washed with acetone. Recrystallization from MeOH−acetone gave **5** (0.035 g, 39%). ^{1}H NMR (DMSO-d_6) δ (ppm) = 10−10.2 (4H, protoporphyrin IX); 8.5, 9.2 (16H, bpy); 6.1, 6.4, 8.5 (6H, vinyl); 3.6, 3.7 (12H, CH_3 on protoporphyrin IX); 3.3−4.3 (12H, $CH_2CH_2COOCH_2$); 4.3−4.4 (10H, CH_3N^+, CH_2N^+); 0.8−1.8 (36H, $-(CH_2)_9-$).

Au-colloids (13 ± 1 nm) were synthesized[22] by the addition of $AuHCl_4 \cdot 3H_2O$ (50 mg) to a rapidly stirred solution of sodium citrate (100 mg) in water (500 mL) at reflux. The solution was then stirred under reflux for an additional 15 min and then allowed to cool slowly to room temperature.

Ultrapure water was used throughout this work and was obtained from a Seralpur PRO 90 CN system. All other materials (Aldrich) were used with no further purification. Electrodes were indium-doped tin oxide (ITO)-coated glass (one side) cut to pieces 20 × 10 mm and 20 × 20 mm for the electrochemical and the photoelectrochemical measurements, respectively. Cleaning and silylation of the electrodes were performed according to the literature.[23] The electrodes were washed with ethanol, sonicated for 15 min in 5% HCl, and washed with ethanol and then with water. Silylation was performed by immersion of the ITO slides into a 2−3% solution of 3-aminopropyltriethoxysilane in ethanol for ∼2 min, after which the electrodes were washed thoroughly with ethanol and then heated to 110 °C for 10 min. Finally, the silylated electrodes were washed with water. The cross-linked Au-nanoparticle arrays were prepared by the alternate immersion of the ITO slides in the Au-nanoparticle suspension for 2 h followed by the immersion of the Au-nanoparticle-functionalized slides in ∼10 mM solution of the dyad (**1** or **2**) for 2 h. After each treatment, the electrodes were washed three times with water. The number of repeated steps used to modify the surface with the Au-nanoparticles and **1** or **2** controlled the number of aggregated layers of Au-nanoparticles associated with the electrodes. Special attention was paid to avoid the drying of the electrode. The electrodes were stored in water, and during electrochemical measurements the lower part, 3−5 mm, of the electrodes was immersed in the electrochemical cell.

Electrochemical Measurements. Electrochemical measurements were performed using a potentiostat (EG&G, VersaStat) connected to a personal computer (EG&G electrochemical software model 270/250). All measurements were carried out at ambient temperature (25 ± 3 °C) in a three-compartment electrochemical cell consisting of the chemically modified electrode as the working electrode, a glassy carbon auxiliary electrode isolated by a glass frit, and a saturated calomel electrode (SCE) connected to the working volume with a Luggin capillary. All potentials are reported with respect to the SCE. Argon bubbling was used to remove oxygen from the electrolyte solutions in the electrochemical cell.

Photoelectrochemical Measurements. Photoelectrochemical experiments were performed with a home-built photoelectrochemical system that includes a 300W Xe lamp (Oriel, model 6258), a monochromator (Oriel, model 74000), and a chopper (Oriel, model 76994). The electrical output from the cell was sampled by a lock-in amplifier (Stanford research model SR 830 DSP) which provides the shutter chopping frequency. The photoelectrode consisted of the ITO-conductive glass modified with a programmed array of layers of **1**- or **2**-cross-linked Au-nanoparticles. A graphite electrode was used as a counter electrode. The photogenerated voltage and current were measured between the working and counter electrodes. In the case of biasing of the photoelectrode with the external potential, a SCE reference was applied. The solution in the photoelectrochemical experiments was

(14) Shipway, A. N.; Lahav, M.; Blonder, R.; Willner, I. *Chem. Mater.* **1999**, *11*, 13−15.
(15) Lahav, M.; Shipway, A. N.; Willner, I. *J. Chem. Soc., Perkin Trans. 2* **1999**, 1925−1931.
(16) Lahav, M.; Shipway, A. N.; Willner, I.; Nielsen, M. B.; Stoddart, J. F. *J. Electroanal. Chem.* **2000**, *482*, 217−221.
(17) Lahav, M.; Gabai, R.; Shipway, A. N.; Willner, I. *Chem. Commun.* **1999**, 1937−1938.
(18) Lahav, M.; Gabriel, T.; Shipway, A. N.; Willner, I. *J. Am. Chem. Soc.* **1999**, *121*, 258−259.
(19) Hu, Y. Z.; van Loyen, D.; Schwarz, O.; Bossmann, S. H.; Dürr, H.; Huch, V.; Veith, M. *J. Am. Chem. Soc.* **1998**, *120*, 5822−5823.
(20) Hu, Y. Z.; Bossmann, S. H.; van Loyen, D.; Schwarz, O.; Dürr, H. *Chem. Eur. J.* **1999**, *5*, 1267−1277.
(21) Saito, T.; Hirata, Y.; Sato, H.; Yoshida, T.; Mataga, N. *Bull. Chem. Soc. Jpn.* **1988**, *61*, 1925−1931.
(22) . Brust, M.; Bethell, D.; Schiffrin, D. J.; Kiely, C. J. *Adv. Mater.* **1995**, *7*, 795−797.
(23) Doron, A.; Katz, E.; Willner, I. *Langmuir* **1995**, *11*, 1313−1317.

Scheme 1: Stepwise Assembly of Three-Dimensional Photosensitizer/Electron Acceptor Au-Nanoparticle Arrays on a Conductive ITO Support

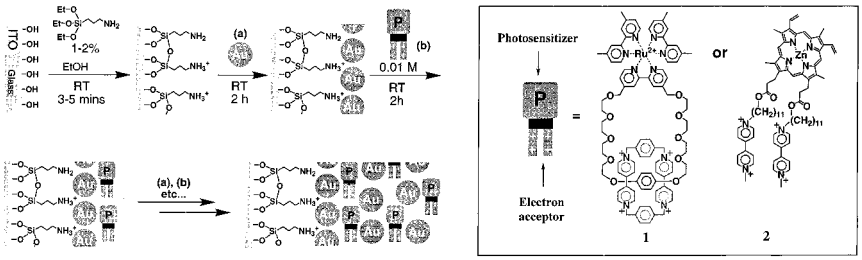

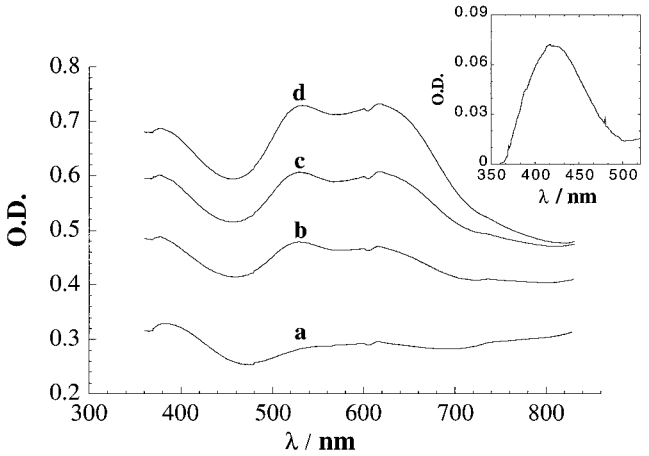

Figure 1. Absorbance spectra of layered **1**-cross-linked Au-nanoparticle arrays on an ITO electrode: (a) One Au-nanoparticle layer. (b) Three Au-nanoparticle layers. (c) Four Au-nanoparticle layers. (d) Five Au-nanoparticle layers. Each of the Au-nanoparticle arrays includes on the last layer the cross-linker **1**. Inset: The absorbance spectrum obtained upon the subtraction of the spectrum of the first Au-nanoparticle layer prior to the association of **1** from the spectrum of the first Au-nanoparticle layer with electrostatically linked **1** (curve a, Figure 1).

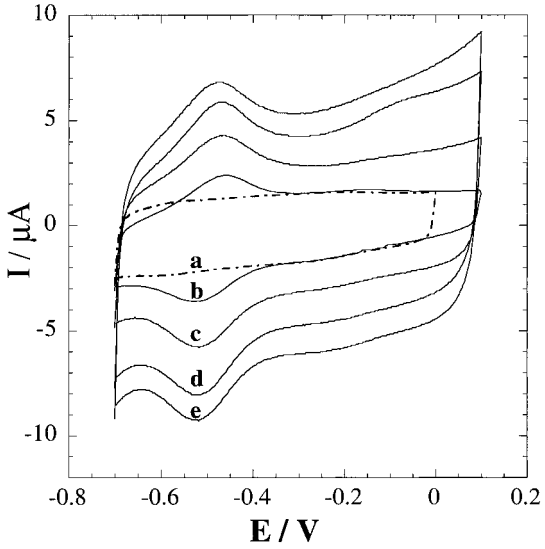

Figure 2. Cyclic voltammograms of layered **1**-cross-linked Au-nanoparticle arrays. Voltammograms correspond to the quasi-reversible redox responses of the bipyridinium unit in the catenane (**1**): (a) Voltammogram of the ITO electrode with a single Au-nanoparticle layer prior to interaction with **1**. (b−e): Au-nanoparticle arrays consisting of one, three, four, and five **1**-cross-linked Au-nanoparticle arrays that include associated **1** on top of the last layer. All data were recorded in 0.1 M phosphate buffer solution, pH = 7.2, scan-rate 100 mV·s^{-1}, under Ar.

composed of 0.1 M Na_2EDTA in 0.1 M phosphate buffer, pH 7.2. An Ar-stream was applied to the photoelectrochemical cell to remove oxygen prior to the photocurrent/photovoltage measurements. The experimental values of the photocurrent were normalized to the number of incident photons at $\lambda = 615$ nm.

Absorbance spectra were measured on a Uvikon 860 (Kontron) spectrophotometer, and the pH values of buffer solutions were determined with a pH-meter (Corning ion analyzer 150).

Results and Discussion

The photophysical properties of the Ru(II)−tris(2,2′-bipyridine)-cyclobis(paraquat-*p*-phenylene) catenane, (**1**), were previously reported.[20] The intramolecular electron-transfer quenching rate-constant was estimated to be $k_q = 2.6 \times 10^7$ s^{-1}. Scheme 1 outlines the method to assemble the **1**-cross-linked Au-nanoparticle array on a conductive ITO glass support. The ITO surface is functionalized with an aminosiloxane layer and citrate-capped Au-nanoparticles (13 ± 1 nm) were self-assembled onto this interface.[23] Electrostatic attractive interactions between the functionalized surface and the citrate-capped Au-nanoparticles were suggested as the driving force for the formation of the nanoparticle layer. The resulting Au-nanoparticle interface was then interacted with a solution of the oligocationic catenane, (**1**), resulting in the association of the photosensitizer−electron acceptor catenane to the Au-nanoparticle interface. The resulting assembly was then reacted with the Au-nanoparticles and then with **1** to yield the **1**-cross-linked aggregate of Au-nanoparticles. By the number of repeated identical steps, an aggregated array with a controllable number of cross-linked layers (shells) is generated. Figure 1 shows the absorbance spectra of the nanoparticle array upon the build-up of the nanoparticle layers. (Note that each curve corresponds to the respective Au-nanoparticle array that includes atop the cross-linking reagent **1**). Figure 1, inset, shows the spectrum of the first Au-nanoparticle layer that includes co-associated **1**, from which the spectrum of the first Au-nanoparticle layer assembled on the aminosiloxane interface is subtracted. The absorbance spectrum $\lambda_{max} = 425$ nm, which is similar to the absorbance of **1** in solution, indicates that the cross-linking reagent binds to the Au-nanoparticles. The build-up of the nanoparticle array is reflected by the increase in the Au-nanoparticle absorbance at $\lambda = 520$ nm. Also, as the number of Au-nanoparticle layers increases, a second absorbance band that is strengthened in its intensity, is observed at $\lambda = 615$ nm. This absorption band was attributed to an interparticle plasmon coupling exciton.[24] Thus, as the aggregate of Au-nanoparticles increases, the coupled plasmon absorbance is enhanced. The absorbance features of the Au-nanoparticle layers are very similar to those observed with the cyclobis(paraquat-*p*-phenylene) as cross-linker, where an almost linear coverage per layer of Au-nanoparticles that corresponds to 5×10^{10} particle·cm^{-2} was observed.[14]

(24) Collier, C. P.; Say Kally, R. J.; Shiang, J. J.; Henrichs, S. E.; Heath, J. R. *Science* **1997**, *277*, 1978−1981.

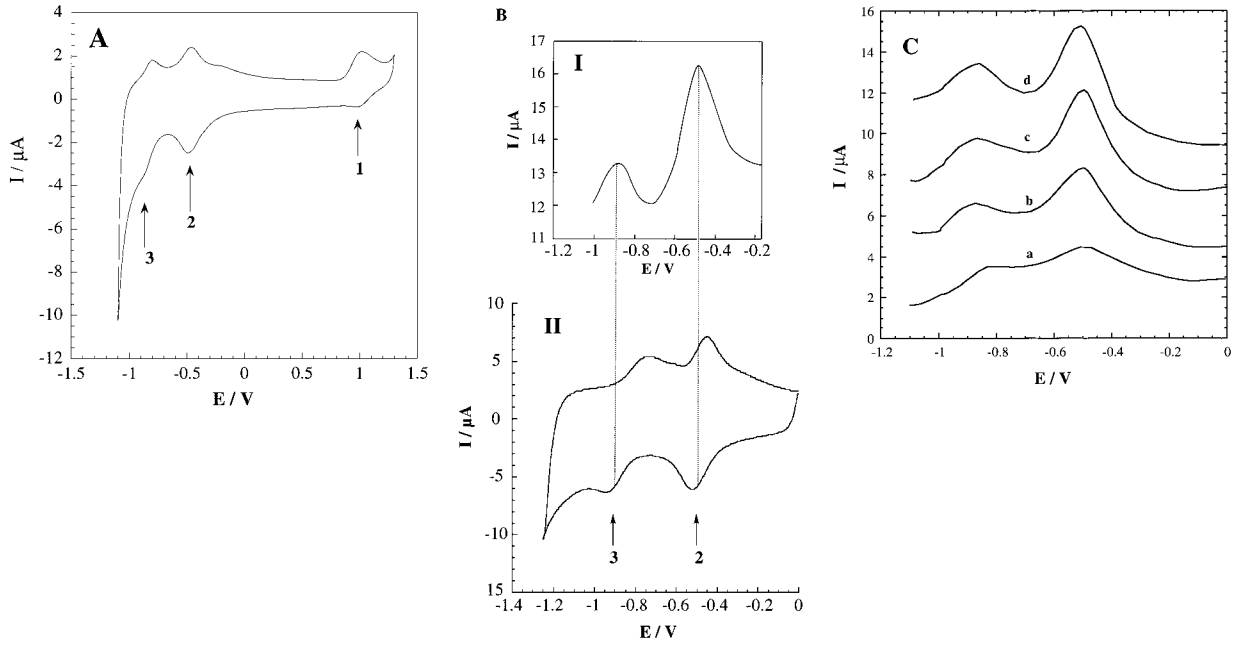

Figure 3. **(A)** Cyclic voltammogram of **1** in a 0.1 M phosphate buffer solution, pH = 7.2, scan rate 100 mV·s^{-1}, under Ar: (1), (2), and (3) indicate the redox-processes outlined in eq 1. **(B)** Differential pulse voltammogram (DPV) of a four-layer array of **1**-cross-linked Au-nanoparticles, Panel I, in comparison to the cyclic voltammogram of **1** in 0.1 M phosphate buffer solution, pH = 9.2, scan-rate 100 mV·s^{-1}, Panel II. The redox waves (2) and (3) correspond to the respective numbered steps in eq 1. **(C)** Differential pulse voltammograms of layered **1**-cross-linked Au-nanoparticle arrays. The voltammograms (a−d) correspond to the one, two, three, and four **1**-cross-linked Au-nanoparticle layers. Data recorded in 0.1 M phosphate buffer solution, pH = 9.2, scan-rate 20 mV·s^{-1}, under Ar.

Figure 2 shows the cyclic voltammograms of the **1**-cross-linked Au-nanoparticle array upon the build-up of the array. The quasi-reversible wave at $E^\circ = -0.45$ V corresponds to the redox process of the interlocked bipyridinium cyclophane. Coulometric analysis of the redox-wave reveals that the charge associated with the bipyridinium units increases almost linearly as the number of layers is elevated. Coulometric assay of the reduction wave of the bipyridinium cyclophane units (or the analysis of the oxidation wave of the respective radical-cation) indicates that the surface coverage of the cross-linking molecules per layer is $\sim 3.6 \times 10^{-12}$ mole·cm^{-2}. This translates to an average surface coverage of ~45 cross-linking units per Au-nanoparticle.

Figure 3A shows the cyclic voltammogram of diffusional **1.** Three quasi-reversible redox-waves are observed, where the redox-wave at $E_1^\circ = \sim 1.0$ V corresponds to the oxidation and reduction of the Ru^{2+}−polypyridine site, eq 1, (step 1) the redox-wave at $E_2^\circ = -0.45$ V, corresponds to the reduction and oxidation of the interlocked bipyridinium cyclophane, eq 1, (step 2), and the redox-wave at $E_3^\circ = \sim -0.9$ V is attributed to the reduction of the Ru^{2+}−tris-bipyridine complex unit, eq 1 (step 3). The resolution of the latter wave is quite low due to the cathodic discharge of the electrolyte solution. The electrochemical assay of the Ru(II)−tris-bipyridine cyclobis(paraquat-*p*-phenylene) catenane (**1**) in the Au-nanoparticle array is, however, difficult. The oxidation of the Au-nanoparticles in the positive potential region prohibits to follow the oxidation process of the Ru(II) complex, eq 1 (step 1). Similarly, the capacitance of the Au-nanoparticle array and the cathodic discharge of the electrolyte, turn the poorly resolved redox-wave corresponding to the reduction of the Ru(II)−tris-bipyridine site, eq 1 (step 3), to be almost invisible in the respective cyclic voltammograms. The availability of the intact **1**, in the Au-nanoparticle array is, however, nicely confirmed by differential pulse voltammetry (DPV) experiments, Figure 3B (panel I) and C. Figure 3B shows the differential pulse voltammogram of a four-layer array of **1**-cross-linked Au-nanoparticle in comparison to the cyclic voltammogram of diffusional **1**. It should be noted that the electrochemical experiments shown in Figure 3B were performed at pH = 9.2 to separate the redox process outlined in step 3, eq 1, from the cathodic discharge of the electrolyte (note that at pH = 7.2 the two processes are overlapping, cf. Figure 3A). One observes in the **1**-cross-linked Au-nanoparticle assembly the redox waves characteristic to the intact photosensitizer−electron acceptor cross-linking units that correspond to the redox reactions outlined in eq 1 (steps 2 and 3). Figure 3C shows the differential pulse voltammograms of **1** upon the build-up of variable numbers of cross-linked Au-nanoparticle layers. The intensity of the redox responses of **1** increases as the number of Au-nanoparticle layers in the assembly is higher.

Scheme 2: Photoinduced Electron Transfer in the Three-Dimensional Photosensitizer/Electron Acceptor Arrays, and Electron Transport for the Generation of Photocurrents

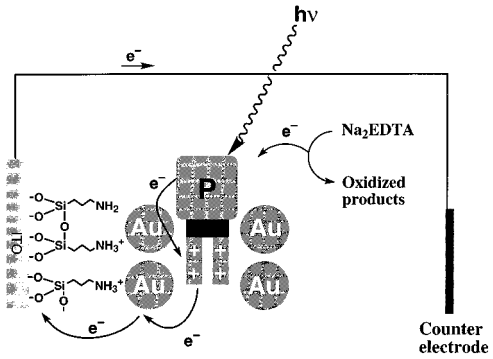

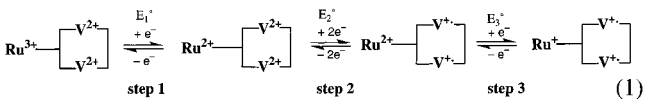

(1)

The photoelectrical output from the cell composed of the photoelectrode and counter electrode was measured upon

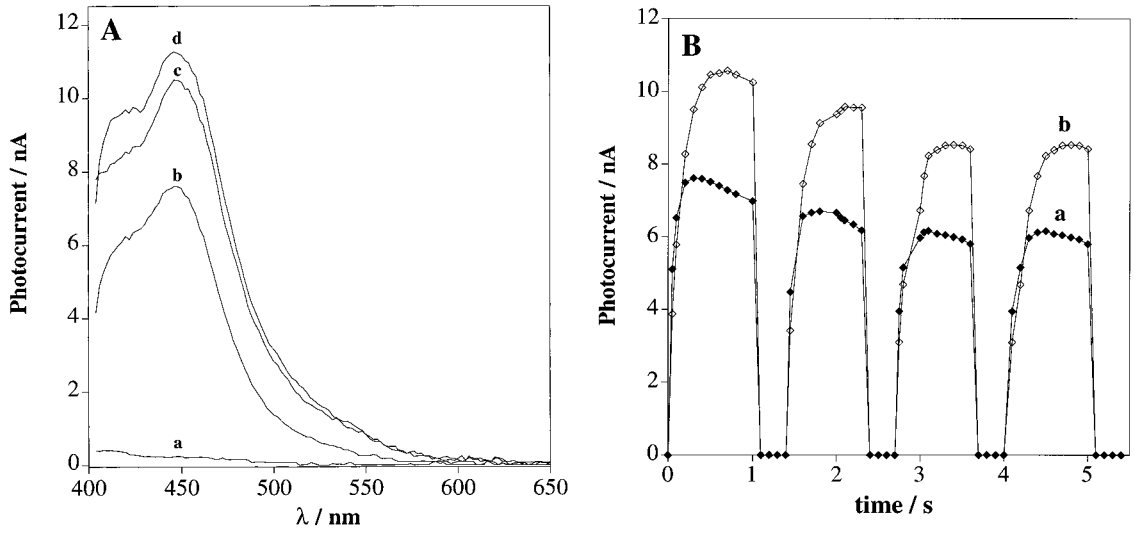

Figure 4. **(A)** Photocurrent action spectra of **1**-cross-linked Au-nanoparticle array on an ITO electrode: (a) ITO electrode functionalized with one layer of Au-nanoparticles prior to the immobilization of **1**; (b), (c), and (d) include one, three, and four **1**-cross-linked Au-nanoparticle layers, respectively. **(B)** Light-induced "ON"-"OFF" switchable photocurrents resulting in (a) one layer and (b) four layers of **1**-cross-linked Au-nanoparticle arrays. Data recorded under Ar.

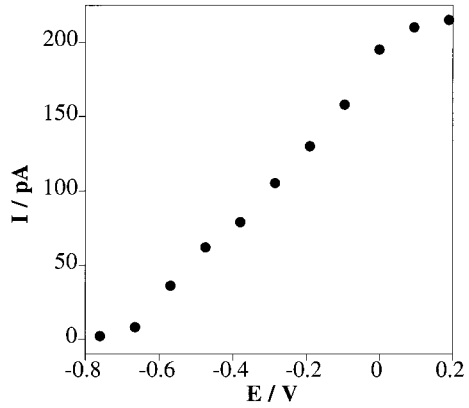

Figure 5. Photocurrents of a four-layer **1**-cross-linked Au-nanoparticle array at different bias potentials applied to the photoelectrode. The electrode was irradiated at $\lambda = 434$ nm, under Ar.

monochromatic irradiation in the presence of a sacrificial electron donor, Na_2EDTA, and under Ar (Scheme 2). Figure 4(A) shows the action spectra corresponding to the resulting photocurrents of cross-linked Au-nanoparticle aggregates that include variable numbers of cross-linked particles. The photocurrent action spectra follow the absorption spectrum of the Ru(II)−tris-bipyridine chromophore with a maximum intensity at $\lambda = 440$ nm, $I_{max} = 11.2$ nA for four layers. The photocurrent increases as the number of cross-linked layers increases. The photocurrent does not, however, increase linearly, and the slope of its increase becomes smaller as the number of Au-nanoparticle layers is elevated, even though the number of Au-nanoparticles and the associated photosensitizer−electron acceptor dyad is almost constant in each cross-linked layer. The enhancement in the photocurrent upon the build-up of the Au-nanoparticle cross-linked array indicates that the aggregated Au-nanoparticles provide electrical wiring paths for the photoejected electrons into the bulk ITO-electrode (vide infra). The nonlinear decrease in the photocurrent magnitude upon the build-up of the layers may be attributed to partial absorption of the light by the Au-nanoparticles and light-scattering by the particles, as well as to defects in electron conduction routes in the Au-nanoparticle array. Figure 4B shows the "ON" and "OFF" photoswitchable photocurrents upon the irradiation of the photosensitizer−electron acceptor Au-nanoparticle cross-linked array.

Figure 5 shows the photocurrent in the system, upon the application of different bias potentials on the electrode. It is evident that no photocurrent is observed when the electrode is biased at $E < -0.6$ V, whereas the photocurrent increases upon biasing the potential on the electrode at $E > -0.6$ V. These results shed light on the mechanism that leads to the development of the photocurrent in the system and on the functions of the bipyridinium catenane in the photoelectrochemical activity of the system. Photoexcitation of the Ru(II)−tris-bipyridine chromophore results in electron transfer to the interlocked bipyridinium cyclophane units, eq 2. Biasing the electrode with

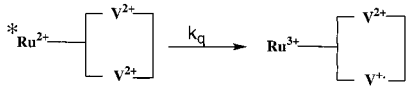

(2)

a potential that is more positive than the redox-potential of the bipyridinium units and realizing that the Au-nanoparticle array exhibits three-dimensional conductivity result in the oxidation of the reduced acceptor and the uptake of the electron by the bulk electrode. This potential-induced scavenging of the reduced photoproducts competes with the intramolecular back electron transfer, eq 3. As the potential turns more positive, scavenging

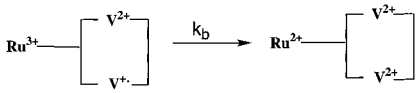

(3)

of the reduced species is more efficient, and at a potential of ~0.0 V all photogenerated redox-species generate the photocurrent. At negative potentials, $E < -0.6$ V all of the bipyridinium sites are reduced, and the photoinduced electron transfer in the photosensitizer−electron acceptor dyad is prohibited, and thus the photocurrent is blocked. These results clearly indicate that the photocurrent is not generated by direct electron transfer from the excited chromophore to the Au-nanoparticles, but it originates from the intramolecular electron transfer in the molecular chromophore−electron acceptor dyad followed by the electrical contacting of the photogenerated redox-species with the electrode by means of the three-dimensional Au-nanoparticle array.

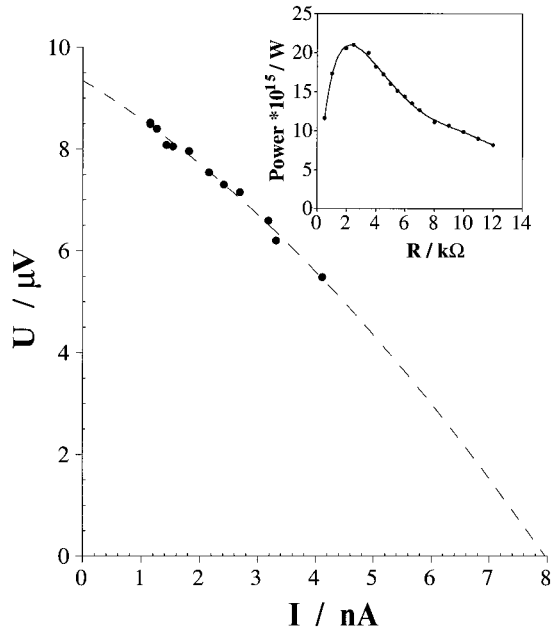

Figure 6. The voltage-current curve developed in the photoelectrochemical cell at different resistance loads. The electrode was irradiated at $\lambda = 434$ nm. (Inset) The power extracted from the photoelectrochemical cell at different resistance loads.

The photocurrent and photovoltage of the photoelectrochemical cell that includes an Au-layer cross-linked electrode were determined at different external resistance loads. Figure 6 shows the voltage−current curve at different resistance loads. Figure 6 inset, depicts the power of the photoelectrochemical cell at different external loads. The maximum power is obtained at an external load of ~3 kΩ, and it corresponds to $\sim 2.1 \times 10^{-14}$ Watt.

To determine the power conversion efficiency by the photoelectrode it is necessary to evaluate the open-circuit voltage conversion efficiency $\phi(U_{oc})$ (eq 4) and the quantum efficiency of current production under the short-circuit condition $\phi(I_{sc})$ (eq 5).[25]

$$\phi(U_{oc}) = U_{oc}/h\nu \quad (4)$$

$$\phi(I_{sc}) = (dn_e/dt)/(dn_{h\nu}/dt) \quad (5)$$

In these equations $h\nu$ is the energy of the absorbed light quantum in electron-volts (eV) (dn_e/dt) and ($dn_{h\nu}/dt$) are the number of photoelectrons produced per second under the short-circuit conditions, and the number of absorbed photons per second, respectively. Since the value of $\phi(U_{oc})$ depends on the energy of the absorbed light quantum it was calculated at the wavelength corresponding to the maximum of the photocurrent action spectrum ($\lambda = 434$ nm; $h\nu = 2.85$ eV). The photovoltage generated under open-circuit condition, U_{oc}, measured upon irradiation at $\lambda = 434$ nm is equal to ~9.4 μV that results in $\phi(U_{oc}) = 3.3 \times 10^{-6}$. Theoretically, U_{oc} can reach the value that corresponds to the difference between the redox potentials of the electron acceptor (bipyridinium cyclophane $E° = -0.45$ V) and electron donor[26] (Na_2EDTA, $E° = \sim 0.4$ V) in the photochemical system.[27] Taking into account these redox potentials, the theoretical limit for the open-circuit voltage conversion efficiency is $\phi(U_{oc}) = 0.3$. The quantum efficiency

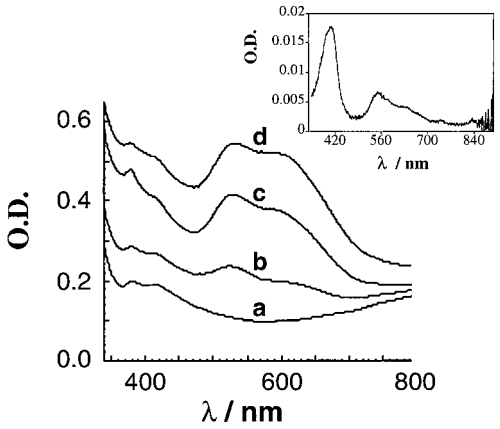

Figure 7. Absorbance spectra corresponding to layered **2**-cross-linked Au-nanoparticle arrays: (a−d) correspond to one, two, three, and four cross-linked layers, respectively. Inset: Absorbance spectrum obtained upon the subtraction of the spectrum of the first layer of Au-nanoparticles prior to the deposition of **2** from spectrum (a) in the figure.

of photoelectron production, $\phi(I_{sc}) = 1 \times 10^{-4}$, was estimated on the basis of the measurement of the absorbed light and the short-circuit photocurrent. The quantum yield of the photoseparated charges[20] between the photosensitizer (Ru-complex) and the electron acceptor (bipyridinium cyclophane) is equal to 4.7×10^{-2}, and it can be considered as the theoretical limit for the photocurrent yield. To determine the power efficiency of light-energy conversion, the photovoltage vs photocurrent dependence for the photoelectrochemical cell was obtained by measuring the photocurrent and photovoltage depending on the load resistance (Figure 6). This voltammetric curve differs from a rectangular pattern characteristic to an ideal electrochemical generator.[25] Its deviation is due to electrochemical polarization of the photoelectrode when the photocurrent is flowing in the circuit. The deviation degree is quantitatively characterized by the fill factor value $f = W_{max} \times I_{sc}^{-1} \times U_{oc}^{-1} = 0.28$, where W_{max} is the maximal power deliverable by the cell equal to 2.1×10^{-14} W at ~3.4 kΩ load resistanace. The power efficiency of the photoelectrochemical cell according to the absorbed light, $\phi(W)$, was calculated in the following way: $\phi(W) = f[\phi(U_{oc})]\text{-}[\phi(I_{sc})] = \sim 1 \times 10^{-10}$. The theoretical limit of the power conversion efficiency for this photoelectrode can be estimated to be $\sim 1.4 \times 10^{-2}$ taking into account the theoretical limits for $\phi(U_{oc})$ and $\phi(I_{sc})$ equal to ~0.3 and 1.4×10^{-2}, respectively, and realizing that the fill factor of the ideal electrochemical generator[25] is equal to 1.

An additional photoactive Au-nanoparticle cross-linked layered electrode for the generation of photocurrents was developed[18] by the application of the Zn(II)-protoporphyrin IX−bis(*N*-methyl-*N*′-undecanoate-4,4′-bipyridinium) (**2**) as photosensitizer−electron acceptor dyad, Scheme 1. The Au-nanoparticle array is constructed by the primary assembly of the Au-nanoparticle layer on a 3-aminopropylsiloxane-functionalized ITO, followed by the sequential association of **2** and again Au-nanoparticles to yield an aggregated cross-linked array that includes a controllable number of Au-nanoparticle shells. Figure 7 shows the absorption spectra of the Au-nanoparticles upon the build-up of the layered array. The plasmon absorbance-band at $\lambda = 520$ nm, characteristic of the Au-nanoparticles increases as the number of layers is elevated with the concomitant formation and growth of a second absorbance band at $\lambda = 620$ nm, characteristic of interparticle coupled plasmon excitons. Figure 7, inset, shows the spectrum that corresponds to the first layer of Au-nanoparticles with surface-associated **2** from which the spectrum of the first layer of Au-nanoparticles was

(25) Quickenden, T. I.; Yim, G. K. *Solar Energy* **1977**, *19*, 283−288.
(26) Katz, E. In *Biological Cycle of Substances and Energy in the System of Soil-Plant*; Gazieiev, A. I., Ed.; Pushchino: Moscow, 1983; pp 26−31
(27) Gomer, R. *Electrochim. Acta* **1975**, *20*, 13-21.

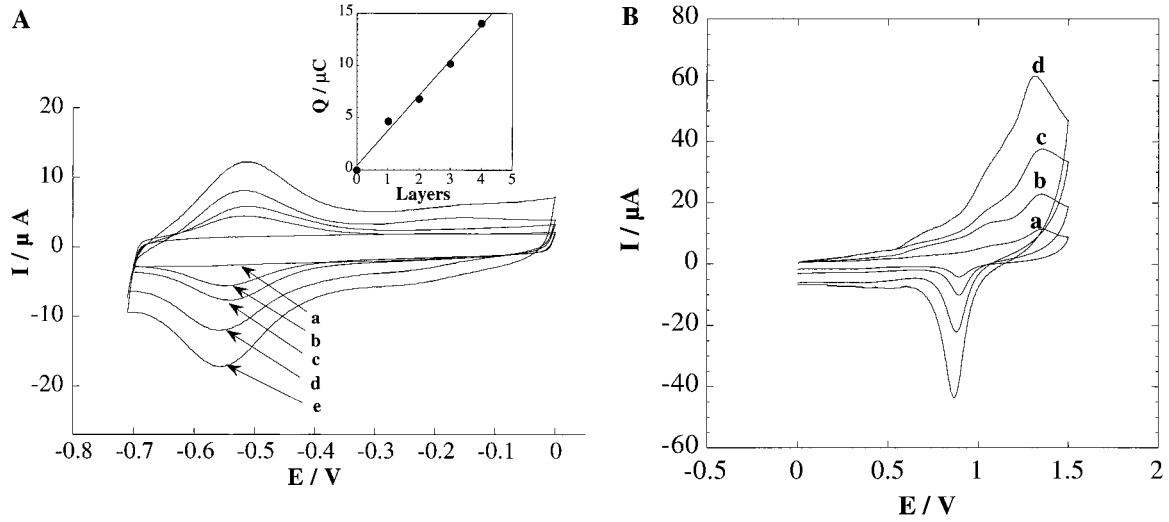

Figure 8. **(**A**)** Cyclic voltammograms of the layered **2**-cross-linked Au-nanoparticle arrays. The voltammograms correspond to the quasi-reversible redox-process of the bipyridinium units: (a) Voltammogram of ITO electrode with one layer of Au-nanoparticles prior to the deposition of **2**; (b−e) one, two, three, and four **2**-cross-linked Au-nanoparticle arrays. Data were recorded in phosphate buffer, pH = 7.2, scan-rate 100 mV·s^{-1}, under Ar. Inset: Build-up of the multilayer array as demonstrated by coulometric analysis of curves (a−e). **(B)** Cyclic voltammograms of **2**-cross-linked Au-nanoparticle arrays: (a−d) correspond to one to four Au-nanoparticle layers. Data recorded in 1 M H_2SO_4, scan-rate 50 mV·s^{-1}.

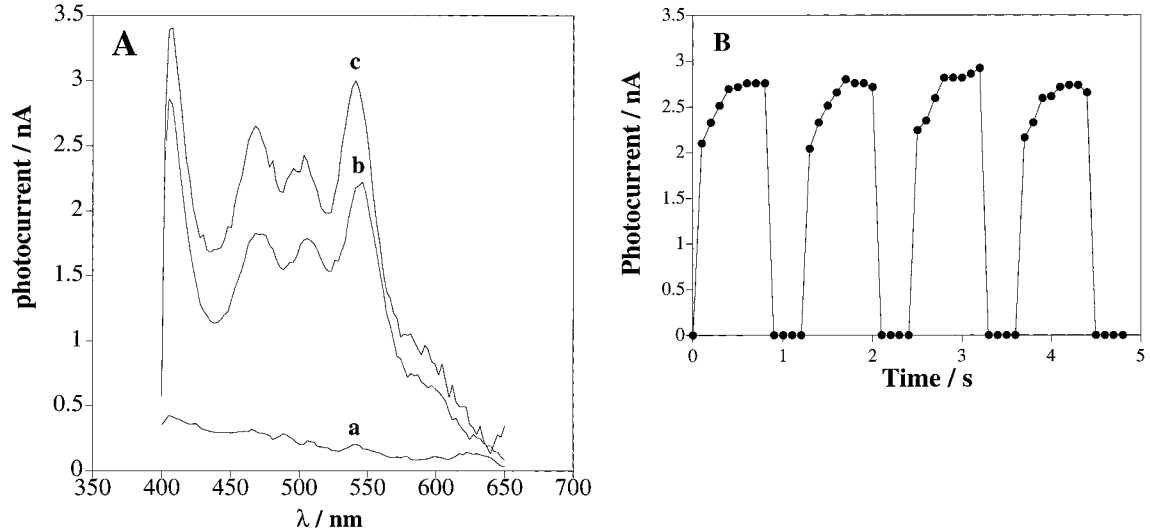

Figure 9. **(**A**)** Photocurrent action spectra of: (a) An ITO glass functionalized with one-layer of Au-nanoparticles prior to interaction with **2**. (b) One layer of Au-nanoparticles with electrostatically adsorbed **2**. (c) A four-layer **2**-cross-linked Au-nanoparticle array on the electrode. **(**B**)** Light-induced "ON" and "OFF" switchable photocurrents for a four-layer electrode. Electrode was irradiated at λ = 544 nm, under Ar.

subtracted. The resulting spectrum corresponds to the Zn−bis-bipyridinium cross-linking dyad, **2**. Due to the nonlinear absorption features of the Au-nanoparticles upon the build-up of the array, it is impossible to follow the dyad absorbances upon the construction of the assembly. The stepwise cross-linking of the Au-nanoparticles by **2**, however, can be characterized by electrochemical means. Figure 8(A) shows the cyclic voltammograms of the cross-linked array upon the build-up of the layers. The quasi-reversible redox-wave of the bipyridinium units is observed at $E^\circ = -0.53$ V. The redox response of the bipyridinium sites increases as the number of cross-linked layers is enhanced. Coulometric assay of the oxidation (or reduction) waves of the bipyridinium units associated with the different layers indicates that the charge associated with the redox-process of the bipyridinium sites increases almost linearly upon the build-up of the array (see inset, Figure 8A), and it corresponds to 3.4 μC per layer. Figure 8B shows cyclic voltammograms of the Au-nanoparticle arrays in 1 M H_2SO_4. The voltammograms consist of the oxidation of the Au-surface ($E \approx 1.35$ V) and a subsequent reduction wave at $E \approx 0.8$ V. Coulometric analysis of the reduction wave allows the calculation of the total gold surface area in each array. One may also observe ill-defined irreversible oxidation waves at ~0.75 and 1.1 V attributed to the oxidation of the Zn-porphyrin cross-linking units. Knowing the size of the Au-nanoparticles (13 ± 1 nm) it is thus possible to calculate the average number of nanoparticles per layer. For example, in the four-layer Au-nanoparticle architecture we estimate the coverage of Au-particles in the top layer to be 0.5 × 10^{11} particles·cm^{-2}. Coulometric analysis of the bipyridinium units in the cross-linker allows the determination that each nanoparticle is associated with an average of 260 molecules of **2**. It should be noted that the Au-nanoparticle arrays that were electrochemically characterized in 1M H_2SO_4 were only used for the characterization of the particles and were not used in any further experiments.

Figure 9A shows the action spectra of the photocurrent resulting from the irradiation of the arrays. The photocurrents increase as the number of cross-linked Au-nanoparticles is

elevated. The photocurrent spectra follow the absorbance pattern of the Zn-protoporphyrin IX chromophore. One may also observe an additional peak at 470 nm. This peak is attributed to the instability of the cross-linking units that undergo demetallization upon irradiation. Figure 9B displays the reversible "ON" and "OFF" activation and deactivation of the photocurrent. The quantum yield of the photocurrent, $\phi(I_{sc})$, is estimated to be $\sim 10^{-3}$ at $\lambda = 544$ nm.

Conclusions

The present study has addressed a novel approach to tailor photoelectrochemically active electrodes by the cross-linking of Au-nanoparticles with different photosensitizer−electron acceptor dyads. The structure, composition, and electrical properties of the three-dimensional Au-nanoparticle arrays were characterized by electrochemical and spectroscopic methods. An important property of the Au-nanoparticle array is the three-dimensional conductivity. An interesting feature of these systems is the fact that the Au-nanoparticle array does not fully quench the excited chromophore. Intramolecular electron transfer in the photoactive dyads generates intermediate redox-species that lead to the generation of the photocurrent. In this context the three-dimensional conductivity of the array is very important since it provides an electrical contacting path between the photogenerated redox species and the bulk electrode. The characterization of the systems reveals that the photocurrent resulting from the cross-linked Au-nanoparticles is controlled by the number of layers associated with the arrays. Albeit, the resulting photocurrents are generated at low efficiency, the method outlined in the present study to fabricate the nanoparticle arrays provides new concepts for the nano-engineering of functional devices. The low efficiencies of the photoelectrochemical cells may be attributed to the energy-transfer quenching of the cross-linking photosensitizers by the Au-nanoparticles. Recent efforts are directed to organize single-electron charging devices,[28] and the nano-engineering of the molecular functionality bridging two conductive nanoparticles is a subject of extensive research. The possibility to couple two nanoparticles, for example, a metallic and a semiconductive, with a photosensitizer−electron acceptor units, opens the way for the future organization of photodriven single electron-transfer devices.

Acknowledgment. This research project is supported by the German-Israel Program (DIP). Parts of the research (H.D.) were supported by the Volkswagen Stiftung, Germany.

JA002568D

(28) Feldheim, D. L.; Grabar, K. C.; Natan, M. J.; Mallouk, T. E. *J. Am. Chem. Soc.* **1996**, *118*, 7640−7641.